

Giant Nonvolatile Electric Field Control of Proximity-Induced Magnetism in the Spin–Orbit Semimetal SrIrO₃

Arun Kumar Jaiswal, Robert Eder, Di Wang, Vanessa Wollersen, Matthieu Le Tacon, and Dirk Fuchs*

With its potential for drastically reduced operation power of information processing devices, electric field control of magnetism has generated huge research interest. Recently, novel perspectives offered by the inherently large spin–orbit coupling of 5*d* transition metals have emerged. Here, nonvolatile electrical control of the proximity-induced magnetism in SrIrO₃ based back-gated heterostructures is demonstrated. Up to a 700% variation of the anomalous Hall conductivity (σ_{AHE}) and Hall angle (Θ_{AHE}) as function of the applied gate voltage V_{g} is reported. In contrast, the Curie temperature $T_{\text{c}} \approx 100$ K and magnetic anisotropy of the system remain essentially unaffected by V_{g} indicating a robust ferromagnetic state in SrIrO₃ which strongly hints to gating-induced changes of the anomalous Berry curvature. The electric-field induced ferroelectric-like state of SrTiO₃ enables nonvolatile switching behavior of σ_{AHE} and Θ_{AHE} below 60 K. The large tunability of this system, opens new avenues toward efficient electric-field manipulation of magnetism.

1. Introduction

Electric field (EF) control of magnetism in materials is of central importance for the development of sustainable and low power consumption information technology.^[1–3] It is particularly challenging to achieve in ferromagnetic (FM) metals in which EF large enough to induce sizeable modifications of the magnetic state can generally not be applied. This has triggered intense research activity in particular on multiferroic oxides, where magnetic and ferroelectric order are inherently coupled, albeit generally weakly, or on heterostructures combining FM metals with a

dielectric or ferroelectric gating material. There, the mechanism for the EF control of magnetism can be based on, e.g., elastic strain mediation in combination with the inverse magnetostrictive effect, on voltage control of exchange coupling,^[1] or a modulation of the charge carrier density.

Latter approach is particularly relevant when magnetic phase, -moment, and -anisotropy depend noticeably on the density of states near the Fermi energy E_{F} but is generally not very efficient in good FM metals. There, the EF-induced modulation of the carrier density n is limited by the Thomas–Fermi screening length $\lambda_{\text{TF}} \propto (1/n)^{1/6}$ which only amounts to about 1 Å.^[4] This has proven more effective in semiconductors^[5] or in transition metal oxides (TMOs)^[1] known for exhibiting significantly smaller n .

In heavier TMOs, such as the 4*d* TMO SrRuO₃, electrostatic modulation of n may not only result in changes of the magnetization and its anisotropy^[6] but can also affect the integral of the Berry curvature (BC), thereby leading to changes of the anomalous Hall effect (AHE)—a fingerprint for the FM state in conductive materials.^[7] AHE originates from the spin–orbit coupling (SOC) which is naturally present in heavy metals and enables, through an asymmetry in the scattering of spin-polarized electrons,^[8] an interplay between spin and charge on the electronic transport at the heart of the emerging field of spin–orbitronics.

SOC is particularly strong in the iridium-based 5*d* TMOs of the Ruddlesden–Popper series Sr_{*n*+1}Ir_{*n*}O_{3*n*+1} in which, however, in contrast to archetypical correlated 3*d* TMOs, the electron–electron correlation strength is generally too small to host ferromagnetism. The iridates display SOC which is on a similar energy scale than that of the electron correlation or electronic bandwidth.^[9] Therefore, they are at the verge of a magnetic ground state and may display AFM or FM properties as well, depending on the details of the Hubbard interaction U and SOC.^[9] The rather large Ir5*d* and O2*p* orbital hybridization in SrIrO₃ (SIO) ($n = \infty$) results in a semimetallic paramagnetic state.^[9–11] We have recently shown that a FM state with large and positive AHE can be induced in SIO by proximity effect when putting it in direct contact with a FM insulator, LaCoO₃ (LCO).^[12] Recent first principle calculations on SIO/LCO heterostructures indicate that it originates from unconventional topology of the electronic band-structure of FM SIO.^[13]

A. K. Jaiswal, R. Eder, M. L. Tacon, D. Fuchs
Karlsruhe Institute of Technology
Institute for Quantum Materials and Technologies
76021 Karlsruhe, Germany
E-mail: dirk.fuchs@kit.edu

D. Wang, V. Wollersen
Karlsruhe Institute of Technology
Institute of Nanotechnology and Karlsruhe Nano Micro Facility
76021 Karlsruhe, Germany

The ORCID identification number(s) for the author(s) of this article can be found under <https://doi.org/10.1002/adfm.202308346>

© 2023 The Authors. Advanced Functional Materials published by Wiley-VCH GmbH. This is an open access article under the terms of the Creative Commons Attribution License, which permits use, distribution and reproduction in any medium, provided the original work is properly cited.

DOI: 10.1002/adfm.202308346

In this work, we demonstrate the EF control of magnetism in SIO heterostructures, evidenced through manifold increases of the anomalous Hall conductivity σ_{AHE} , the Hall angle Θ_{AHE} and the magnetoresistance. We further show that a nonvolatile EF switching behavior is enabled by the EF-induced ferroelectric state of STO. The effects are discussed in terms of Rashba effect at the SIO/LCO interface and topological BC features of the SIO band structure, and we argue that the latter are more likely to account for the experimental observation.

2. Results and Discussion

2.1. Nonvolatile Electrostatic Gating of SrIrO₃

Three terminal back-gating devices consisting of epitaxial SIO/LCO heterostructures were prepared by pulsed laser deposition and photolithography, see the Experimental Section and Figure S1, Supporting Information S1. SIO and LCO film thicknesses of 10 monolayers demonstrate stable and reproducible proximity-induced ferromagnetism in SIO. A scheme of the device layout is shown in **Figure 1a**. The high degree of crystallinity at the SIO/LCO interface is documented by the high-resolution scanning transmission electron microscopy (HR-STEM) micrograph in **Figure 1b**. A gate-voltage $V_g > 0$ (< 0) usually results in an electron accumulation (electron depletion) in the SIO channel. The expected charge carrier modulation Δn induced by electrostatic gating can be estimated by assuming a parallel-plate

capacitor model to be of the order of 0.35% (Supporting Information S1). The modulation thickness of the SIO channel is in principle limited by the Thomas–Fermi screening length^[4], λ_{TF} , which can be significantly larger in semimetals than in good metals due to increased dielectric permittivity (Supporting Information S1). In addition, charge carrier localization may increase λ_{TF} considerably as well. In LCO/SIO heterostructures, the first 6 SIO layers show insulating behavior.^[12] Therefore, even for the rather short $\lambda_{\text{TF}} \approx 0.92$ ML as deduced from experiment, a distinct electric field can be expected at the SIO/LCO interface (Figure S4, Supporting Information S1).

In **Figure 1c**, the relative change of the SIO resistance, $\Delta R/R$, is shown for V_g -sweeps at different temperatures T . $\Delta R/R$ increases with increasing V_g . The positive field coefficient ($dR/dV_g > 0$) suggests a hole-dominated conductivity in contrast to the generally observed negative Hall coefficient which hints to an electron-type transport.^[14–16] This can be accounted for by the different mobilities of the electron and hole charge carriers demonstrated by magnetotransport^[16] and electronic Raman scattering.^[17] Note that electron- and hole-like pockets of semimetallic SIO sensitively depends on the structural properties (epitaxial strain).^[11,14]

The increase of $\Delta R/R$ at any V_g with decreasing T is consistent with the increase of the dielectric constant of STO, ϵ_g . We obtain $\Delta R/R \approx 15\%$ at $T = 2$ K for $V_g = 50$ V, which is larger than what is expected from simple electrostatics consideration and indicates decrease of electron mobility for electron accumulation in SIO/LCO (Figure S2, Supporting Information S1). Weak charge

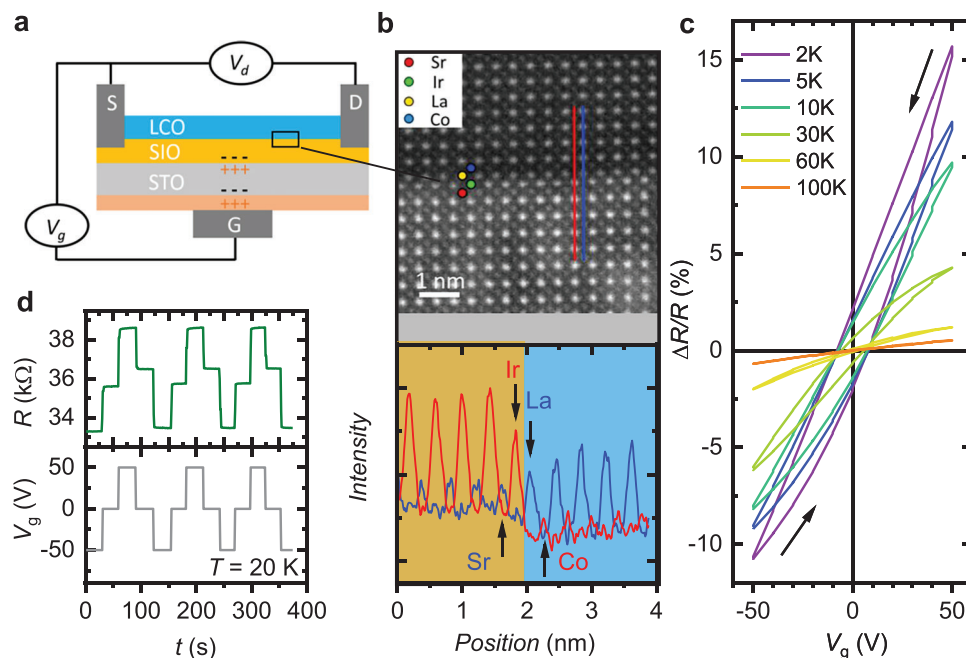


Figure 1. Electrostatic gating of a SIO/LCO heterostructure. a) Scheme of the three terminal gating device structure. Source (S) and drain (D) contacts to the SIO/LCO interface were done by Al-wire bonding. The gate contact (G) was done by Pt-sputtering, silver paint, and Al-wiring. As indicated, a positive gate voltage (V_g) usually results in a negative charging of the SIO channel. b) (Top) Cross-sectional HR-STEM micrograph of a typical SIO/LCO interface. Cations are indicated. The interface displays stoichiometric composition without distinct structural defects. Element line-scans are indicated and shown below. (Bottom) Element line-profiles generated from the cross-sectional HR-STEM. Scan direction (position) is from SIO to LCO. The red (blue) line verifies the atoms on the B- (A-) site of the ABO_3 -perovskite structure, i.e., Ir (Sr) and Co (La). Elements are indicated. c) Variation of the channel resistance during sweeps of V_g at different temperatures. Nonlinear and nonvolatile hysteretic behavior appears below about 60 K. Arrows indicated V_g -sweeping direction. d) Dynamic switching behavior (top) for a specific V_g -sequence (bottom) at 20 K.

carrier localization also likely contributes to the monotonous increase of R with decreasing T ,^[12] and explains the distinct increase of λ_{TF} .

At low temperatures, $\Delta R/R$ displays a nonlinear and hysteretic behavior upon sweeping V_g , akin to gating effects reported in other STO heterostructures.^[18] As such, the resistive state for $V_g = 0$ depends on the history (sweeping direction). The effect is only seen for $T \leq 60$ K, the temperature below which STO undergoes a phase transition to a ferroelectric-like state under electric fields $E \geq 2$ kV cm⁻¹.^[19,20] The applied field strength ($E_g = \pm 5$ kV cm⁻¹) here is large enough to induce such transition and is therefore likely responsible for the observed and well-reproducible nonvolatile switching behavior (Figure 1d).

2.2. Electric Field Control of Magnetism

We now turn to magnetotransport of the thin SIO layer. The insulating character of LCO confines electric transport solely to SIO and allows unambiguous selective characterization of the proximity-induced FM state in SIO.^[12] The AHE and the anisotropic magnetoresistance (AMR), two hallmarks of a FM metal, are related to the structure and ordering temperature of the FM state and are therefore useful quantities to characterize the magnetic properties of the material. The Hall resistivity $\rho_{xy}(\mu_0 H)$ and the magnetoresistance $MR = [\rho_{xx}(\mu_0 H) - \rho_{xx}^0] / \rho_{xx}^0$ ($\rho_{xx}^0 = \rho_{xx}(\mu_0 H = 0)$) with magnetic field $\mu_0 H$ applied perpendicular to the film surface are displayed in **Figure 2** for different V_g at $T = 20$ K, i.e., in the FM state of SIO ($T_C \approx 100$ K). For other temperatures, see the Figure S6, Supporting Information S1.

The total Hall resistivity of SIO, $\rho_{xy}(\mu_0 H)$ can be decomposed in two components, respectively, ordinary (ρ_{OHE}) and anomalous (ρ_{AHE}). ρ_{OHE} is caused by Lorentz force and varies linearly with $\mu_0 H$ within the investigated field range. The large hysteresis seen in ρ_{xy} (Figure 2a) results from the anomalous contribution, typical for a FM metal.^[21] In conventional magnetic systems, ρ_{AHE} is proportional to the perpendicular magnetization M , $\rho_{AHE} = R^A \times M$, where R^A depends on the longitudinal conductivity σ_{xx} .^[22] On this basis, we can well describe our data using the empirical formula $\rho_{xy} = R^O \times H + R^A \times M$, where $M = (M_s \times \tanh(h \times (H \pm H_c)))$ is modeled using a modified Heaviside-step function. Here M_s , h , and H_c are the saturation value, the slope at H_c and the coercive field, respectively. ρ_{AHE} is obtained after subtraction of the field-linear part contribution to $\rho_{xy}(\mu_0 H)$ and is shown in Figure 2b (for ρ_{OHE} see Figure S6, Supporting Information S1).

Remarkably, we observe a strong dependence of ρ_{AHE} with V_g , from which we extract a relative increase of M_s : $(M_s(V_g) - M_s(0)) / M_s(0)$ by a factor of 7 when going from $V_g = -50$ to $+50$ V. A significant increase is also observed for H_c and the saturation field H_s .

The MR obtained from longitudinal resistivity $\rho_{xx}(\mu_0 H)$ at 20 K (see Figure 2c) exhibits strong dependence with V_g alike. It is also well described by the sum of two contributions, the classical Lorentz scattering ($MR \propto H^2$)^[23] resulting in a positive contribution and spin-flip scattering ($MR \propto -M^2$), which contributes negatively to MR in the FM state.^[24] For $V_g = +50$ V MR is dominated by the negative hysteretic contribution confirming strong FM character, in strong contrast to $V_g = -50$ V where MR is bestridden by the classical positive contribution. For $\mu_0 H = 14$ T and $V_g = \pm 50$ V MR amounts to -0.2% (0.4%).

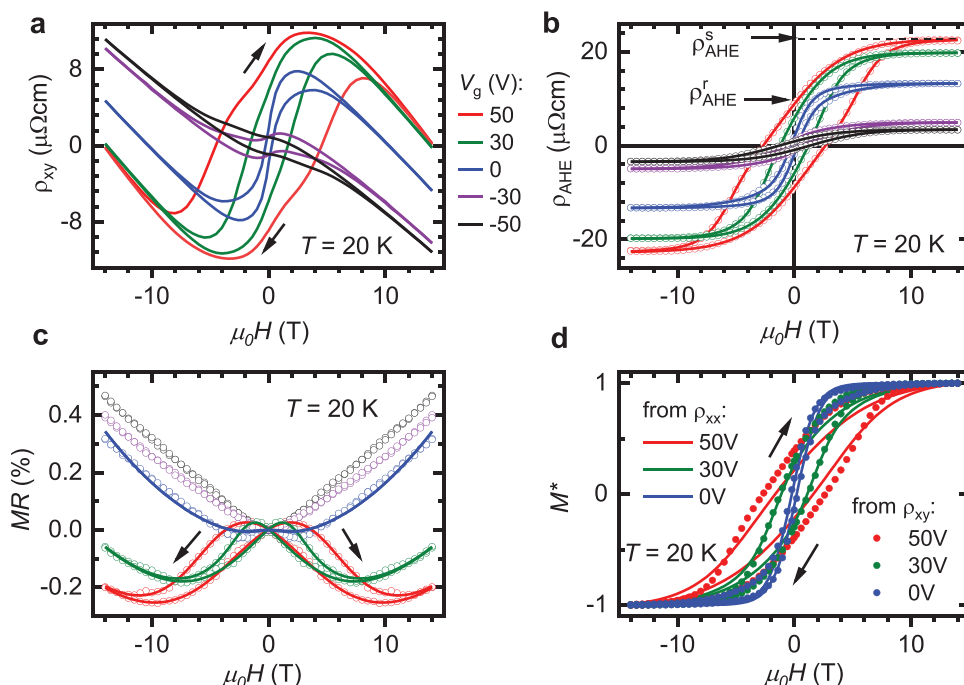


Figure 2. Electric-field dependence of the magnetotransport. a) Hall resistivity ρ_{xy} versus magnetic field $\mu_0 H$ for different V_g at $T = 20$ K. b) The extracted anomalous part of the Hall resistivity ρ_{AHE} (symbols). Fits to the data (see text) are shown by solid lines. ρ_{AHE}^s and ρ_{AHE}^r define the saturated and remnant value of ρ_{AHE} . c) The magnetoresistance MR versus $\mu_0 H$ for different V_g at $T = 20$ K. d) The normalized perpendicular magnetization $M^* = M(\mu_0 H) / M_s$ as derived from the AHE and MR versus $\mu_0 H$ for $V_g > 0$. Arrows indicate the field-sweep direction and color V_g .

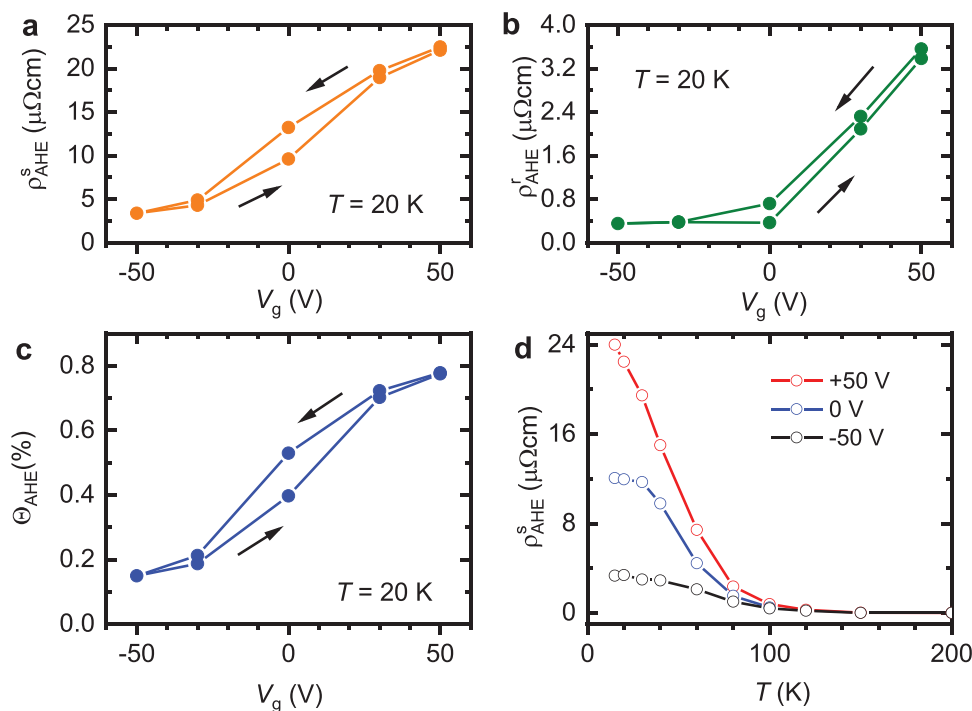


Figure 3. Control of the ferromagnetic state by electrostatic gating. a) The saturated and b) remnant anomalous Hall resistivity $\rho_{\text{AHE}}^{\text{s}}$ and $\rho_{\text{AHE}}^{\text{r}}$ versus V_{g} at $T = 20$ K. c) The Hall-angle $\Theta_{\text{AHE}} = \sigma_{\text{AHE}}^{\text{s}}/\sigma_{\text{xx}}^0$ versus V_{g} at $T = 20$ K. Arrows indicate the field-sweep direction. d) $\rho_{\text{AHE}}^{\text{s}}$ versus T for different V_{g} .

As for the Hall effect, we can extract M from the MR data using a Heaviside step-function to model M and fit the data, albeit only reliably for $V_{\text{g}} > 0$. The “effective magnetization” M perpendicular to the film-plane obtained this way is very similar to that obtained from AHE, as shown on a normalized scale in Figure 2d. It is worth noting that this is not a trivial result as many different mechanisms—intrinsic (integral of the Berry curvature over occupied states^[25]) as well as extrinsic (side-jump- and skew-impurity scattering^[26]) can contribute to the AHE. For our SIO/LCO heterostructures the AHE was found to be intrinsic.^[12]

Next, we take a closer look at the control of the FM state in SIO by electrostatic gating. In Figure 3a,b, we show the saturated and the remnant anomalous Hall resistivity $\rho_{\text{AHE}}^{\text{s}} = \rho_{\text{AHE}}(\mu_0 H = 14\text{T})$ and $\rho_{\text{AHE}}^{\text{r}} = \rho_{\text{AHE}}(\mu_0 H = 0)$, (see also Figure 2b) versus V_{g} . The increase of $\rho_{\text{AHE}}^{\text{s}}$ with V_{g} is nonlinear and indicates the onset of a saturation for $|V_{\text{g}}| > 50$ V.

The field sweep shows hysteretic behavior due to the hysteretic gating effect of the ferroelectric-like STO, see Figure 1c. As already mentioned, sweeping V_{g} from -50 to $+50$ V increases $\rho_{\text{AHE}}^{\text{s}}$ by a factor of 7, while $\rho_{\text{AHE}}^{\text{r}}$ increases by more than one order of magnitude. To the best of our knowledge, and in contrast to reports in, e.g., 4d TMO SrRuO₃ and SrRuO₃/SIO heterostructures, the dependence of the “effective magnetization” with V_{g} reported here is remarkably large.^[7,27,28] Note that the unipolar electrostatic gating asymmetry of the effect for $\rho_{\text{AHE}}^{\text{r}}$ which is less affected for $V_{\text{g}} < 0$ (in contrast to $\rho_{\text{AHE}}^{\text{s}}$) than for $V_{\text{g}} > 0$ might be of practical interest for the realization of spintronic devices.

Another quantity which is also highly relevant for spintronic purposes is the ratio between the saturated anomalous Hall conductivity $\sigma_{\text{AHE}}^{\text{s}} = \rho_{\text{AHE}}^{\text{s}}/[(\rho_{\text{AHE}}^{\text{s}})^2 + (\rho_{\text{xx}}^0)^2]$ and the longitudinal con-

ductivity $\sigma_{\text{xx}}^0 = \rho_{\text{xx}}^0/[(\rho_{\text{AHE}}^{\text{s}})^2 + (\rho_{\text{xx}}^0)^2]$ which defines the anomalous Hall angle $\theta_{\text{AHE}} = \sigma_{\text{AHE}}^{\text{s}}/\sigma_{\text{xx}}^0 = \rho_{\text{AHE}}^{\text{s}}/\rho_{\text{xx}}^0$. Generally, due to the large SOC, θ_{AHE} is much larger in the 5d iridates compared to 3d TMOs.^[22,29] In Figure 3c, θ_{AHE} is shown versus V_{g} for $T = 20$ K. The gate voltage dependence is very similar to that of $\rho_{\text{AHE}}^{\text{s}}$, indicating a much stronger influence of V_{g} on $\rho_{\text{AHE}}^{\text{s}}$ than on ρ_{xx}^0 . This is in full agreement with the intrinsic nature of the AHE in SIO,^[12] where σ_{AHE} does not depend on σ_{xx} . Sweeping V_{g} from -50 to $+50$ V, increases θ_{AHE} by more than 500%. The temperature dependence of M expressed by $\rho_{\text{AHE}}^{\text{s}}(T)$ is shown in Figure 3d for different V_{g} . Although $\rho_{\text{AHE}}^{\text{s}}(T)$ is significantly enhanced for positive V_{g} , the onset of the effect $T_{\text{C}} \approx 100$ K is not much affected by V_{g} .

2.3. Anomalous Magnetoresistance and Magnetic Anisotropy

Manipulation of the magnetic anisotropy or even switching of the magnetic easy-axis from in- to out-of-plane is of special practical interest. In the following, we discuss the EF-dependence of the magnetic anisotropy.

The proximity-induced magnetism of SIO results in an angle-dependent anisotropic magnetoresistance $\text{AMR}(\alpha) = [\rho_{\text{xx}}(\alpha) - \rho_{\text{xx}}(90^\circ)]/\rho_{\text{xx}}(90^\circ)$ below T_{C} , where α is the angle between the in-plane magnetic field- and current-direction (Figure 4b).

Figure 4a displays $\text{AMR}(\alpha)$ for different V_{g} at 20 K and 14 T. Local maxima are seen close to 0° , 90° , 180° , and 270° , with amplitude that strongly depend on V_{g} . This can be described combining a two- and a fourfold angle-dependent component: $\text{AMR}(\alpha) = C_0 + C_2(\alpha) + C_4(\alpha)$, where $C_2(\alpha) = \langle C_2 \rangle \times \cos(2\alpha - \omega_2)$

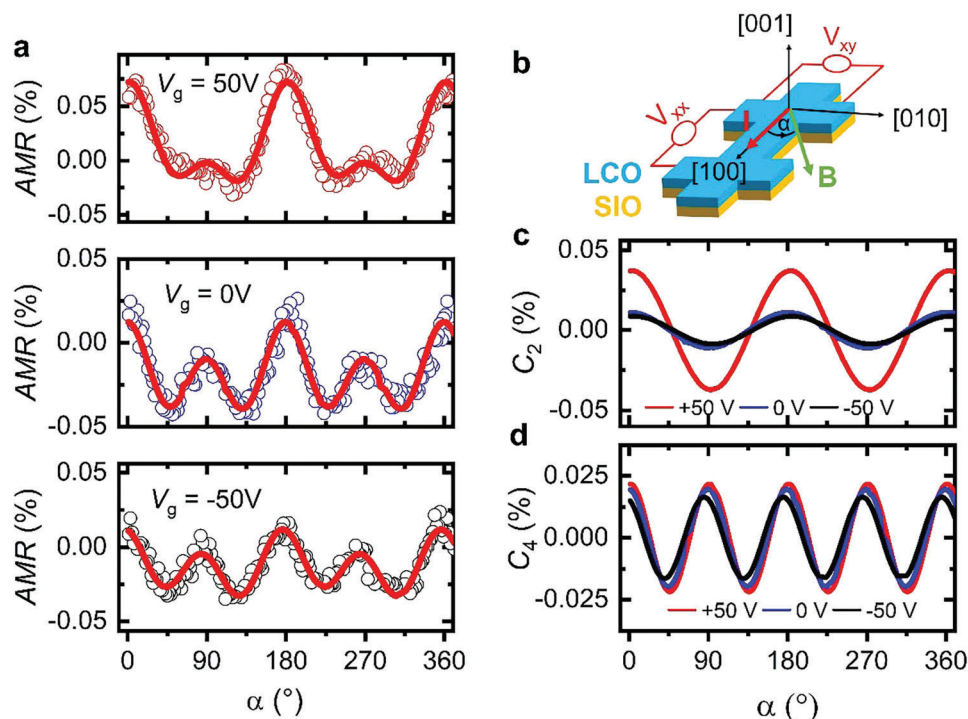


Figure 4. Anomalous magnetoresistance of the SIO/LCO heterostructure. a) The angle-dependent anisotropic magnetoresistance $AMR(\alpha)$ for different V_g at $T = 20$ K and 14 T. b) Schematic of the pseudocubic crystallographic- and in-plane magnetic field direction with respect to the current flow direction. c) The twofold. d) The fourfold component of $AMR(\alpha)$, shown in (a). Fitting parameters are listed in the Supporting Information S1.

and $C_4(\alpha) = \langle C_4 \rangle \times \cos(4\alpha - \omega_4)$. C_0 , $\langle C_2 \rangle$, and $\langle C_4 \rangle$ correspond to the amplitude of each component (offset angles ω_2 and ω_4 are allowed for each of them to account for backlash of the sample rotator).

The twofold component shows maxima at $\alpha = 0^\circ$ and 180° , whereas the fourfold component displays minima at $\alpha = 45^\circ + (n \times 90^\circ)$, $n = 0, 1, 2$, and 3. Fits to the data are shown by solid lines (for fitting parameters, see Table S3, Supporting Information S1). The extracted two- and fourfold components of $AMR(\alpha)$ are shown in Figure 4c,d, respectively.

The angle-dependence of the twofold component is similar to that of the classical $AMR(\alpha)$,^[30] the spin-Hall magnetoresistance, $SMR(\alpha)$,^[31] or the spin-orbit magnetoresistance, $SOMR(\alpha)$.^[32] However, the amplitude of $\approx 0.04\%$ is about two orders of magnitude larger compared to values generally reported for $SMR(\alpha)$ and $SOMR(\alpha)$ ^[31,32] and more typical for the normal $AMR(\alpha)$, where the amplitude depends on the effective magnetization of the sample. This is confirmed by the strong increase of $\langle C_2 \rangle$ by a factor of 5 with increasing V_g , strongly reminiscent of the behavior of ρ_{AHE}^S (so of M).

The fourfold component, on the other hand, does not depend on current direction and is thus related to the magnetocrystalline anisotropy. The minima positions correspond to reduced spin-flip scattering and indicate an in-plane $\langle 110 \rangle$ magnetic easy-axis direction.^[12] In comparison, $\langle C_4 \rangle$ changes only by a factor of 1.6 when V_g is increased which indicates slightly enhanced $\langle 110 \rangle$ -easy-axis behavior. The minima positions of the fourfold magnetocrystalline component are obviously not affected by V_g . The measurements suggest negligible influence

of V_g on the symmetry or strength of the magnetocrystalline anisotropy.

2.4. Discussion

We have presented a series of experimental results demonstrating efficient EF-control of the magnetic behavior of SIO-based heterostructures. Very large changes of ρ_{AHE} ($\times 7$) and Θ_{AHE} ($\times 5$) when sweeping the gate voltage from $V_g = -50$ to $+50$ V are observed, with a strong asymmetry of the effect, which is essentially occurring for $V_g > 0$. In contrast, the magnetic anisotropy and T_C are rather unaffected. Note that in a Stoner description of SIO ferromagnetism, one could expect T_C to be sensitive to changes of the charge carrier density Δn upon gating. Given the weakness of the electrostatic modulation ($\Delta n/n \approx 0.35\%$, see Supporting Information S1) in this system, the variation of T_C might simply be too small to be detected.

How to understand in this context the huge EF-induced changes of the AHE? Two natural options are the EF-dependence of the Rashba effect at the SIO/LCO interface^[33–36] on the one hand and topological features of SIO band structure on the other hand.

The strength of the Rashba effect can be controlled by an applied strong EF through the linear dependence of the Rashba coefficient α_R on E for free charge carriers.^[37] In order to obtain significant effects, large electric field strengths of the order of V/nm have to be applied.^[33] Such a large EF may also result in a strong coupling to electronic structure via orbital deformation

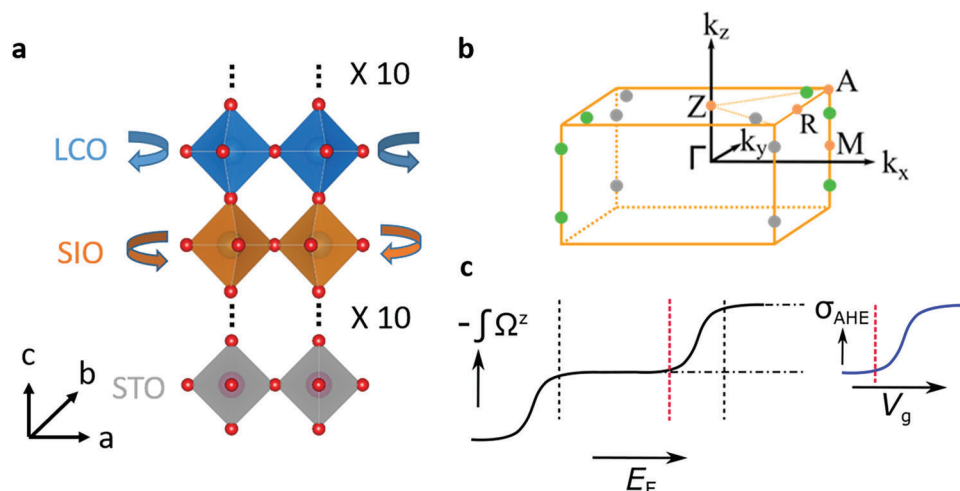


Figure 5. Structure and topology of FM SIO and influence on the AHE. a) Structure of the SIO/LCO heterostructure. Only the pseudocubic perovskite cells are indicated. In-plane lattice parameters are the same as for STO substrate. Out-of-plane lattice parameter of SIO (LCO) is larger (smaller) compared to that of STO. The ($a^0a^0c^-$) octahedral rotation pattern of LCO and SIO is indicated by arrows. b) The Brillouin zone of the tetragonal distorted FM SIO. High symmetric points are indicated. Weyl points with positive (green) and negative (gray) chirality are highlighted. Data were taken from ref. [13]. c) Integral of the BC as a function of E_F . Weyl crossing points occurring 20 meV below E_F (indicated by black dashed line) result in a strong increase of $-\int \Omega^z$. Similar behavior is expected when E_F (indicated by red dashed line) is further increased above the second double of Weyl points located 10 meV above. An increase of V_g and n also increases E_F resulting in a similar rise of σ_{AHE} compared to that of $-\int \Omega^z$ which is shown on the right.

and anomalous band splitting.^[38] The resulting momentum dependent “Rashba equivalent” magnetic field is expected to affect σ_{AHE} quadratically (so symmetrically) on E_F or V_g ,^[33] in strong contrast with our experimental observation, ruling out Rashba origin as the main source for the E_F tunability of the AHE reported here. Note, electric field strength applied here is only of the order 10^{-4} V nm $^{-1}$.

Topological band properties of SIO may also contribute to the AHE. The scattering-independent intrinsic contribution to the AHE comes from the Berry phase supported anomalous velocity. An interesting aspect of the intrinsic contribution to the AHE is that the Hall conductivity σ_{AHE} is given as an integral of the BC, Ω^z , over all occupied states below the Fermi energy^[39]

$$\sigma_{\text{AHE}} = -\frac{e^2}{\hbar} \int \frac{dk}{(2\pi)^3} f(\epsilon_k) \Omega^z \quad (1)$$

Here, $f(\epsilon_k)$ is the Fermi–Dirac distribution function.

A direct connection between BC and magnetotransport has been recently reported for topological insulator Bi $_2$ Se $_3$ ^[40] in which gating-induced upshift of E_F was found to increase the contribution of conduction electrons to BC and to increase the spin Hall conductivity. In magnetic oxides with complex band structures, the intrinsic mechanism for the AHE and the spin Hall effect (SHE) is the same^[22] and depends on the detailed properties of the momentum-space BC. The presence of band crossing points close to E_F can affect the BC and even result in a sign-change of the AHE.^[41]

For SIO, the large intrinsic SHE previously reported^[42,43] supports the existence of BC anomalies. Furthermore, recent first principle calculations on SIO/LCO heterostructures unraveled a ferromagnetic band structure for the tetragonal structured SIO exhibiting nontrivial topological features (double Weyl points above and below E_F) responsible for a large AHE.^[13] Their lo-

cation in the Brillouin zone of the tetragonal distorted FM SIO is shown in **Figure 5b**. They indeed contribute positively to the AHE and the integral BC results in $\sigma_{\text{AHE}} = 7.5 \Omega^{-1} \text{ cm}^{-1}$, well comparable to the experimental value of $3 \Omega^{-1} \text{ cm}^{-1}$ for SIO/LCO below 30 K.^[12]

This allows us to sketch a scenario for the E_F control of magnetism in SIO reported here: since double Weyl points are located only 10 meV above E_F , an E_F -induced charge carrier accumulation ($V_g > 0$) may shift E_F across those band-crossing points (indicated by the dashed black lines in **Figure 5c**). The shift of E_F can be estimated by the electron doping $\Delta n = 3.5 \times 10^{18} \text{ cm}^{-3}$ for $V_g = +50$ V (see the Supporting Information S1) and the density of states (DOS) at E_F (see the Supporting Information of Ref. [13]). Considering the integrated density of states, a shift of 0.01 eV by Δn and therefore access of the second Weyl point by electric gating is very likely. When this occurs, the integral BC increases abruptly and so do σ_{AHE} or Θ_{AHE} .^[44,45] The minor influence of V_g on the magnetic ordering temperature T_C and anisotropy tend to favor such topology-based scenario.^[45]

Many properties such as the orbital magnetization and anomalous Hall conductivity can be expressed in terms of Berry phases, connections, and curvatures and are therefore directly related to each other. Hence, $\rho_{xx}(\mu_0 H)$ and MR will naturally be affected by the AHE alike.^[46] As such, the direct relation between $\rho_{\text{AHE}}(\mu_0 H)$ and MR emphasized earlier (**Figure 2d**) also favors the topological scenario.

3. Conclusion

In summary, we have shown that electrostatic gating allows for a very large tunability of the proximity-induced σ_{AHE} , Θ_{AHE} and MR in SIO/LCO heterostructures likely rooted by the singular band structure of SIO. The results demonstrate that the magnetic properties of FM topological materials can be very effectively

controlled by electric fields, offering a promising avenue for realizing energy efficient spintronic devices.

4. Experimental Section

Sample Preparation: The SIO/LCO heterostructures were grown on (001) oriented SrTiO₃ (STO) substrates by pulsed laser deposition. First, 10 MLs of SIO were deposited on TiO₂-terminated (001)-oriented STO substrate, followed by the deposition of 10 MLs of LCO. Film-thickness and layer-by-layer growth were controlled in-situ by reflection high energy electron diffraction (RHEED). More details on film preparation are described elsewhere.^[12,47] After film preparation, microbridges (40 μm width and 200 μm length) were patterned by standard ultraviolet photolithography and Ar-ion etching. Next, the STO substrate was thinned down from the backside to about 0.1 mm to increase possible electric field strength. The back-gate electrode was provided by Pt-sputtering, silver-paste and Al-wiring, whereas source and drain contacts to the SIO/LCO interface were done by ultrasonic Al-wire bonding.

The structural properties of the SIO/LCO heterostructures were analyzed by X-ray diffraction using a Bruker D8 DaVinci diffractometer and high-resolution transmission electron microscopy (HRTEM) as shown elsewhere.^[12]

Electronic Transport and Data Analysis: Measurements of the electronic transport were carried out using a physical properties measurement system (PPMS) from Quantum Design. The modulated (2 Hz) source-drain sample current was typically 1–10 μA. A sample rotator HR-133 was used for angle-dependent magnetoresistance measurements. The gate-voltage was provided externally by a Keithley 6517B Electrometer, constrained to 50 V by the PPMS. Before the measurements, the sample were kept for 12 h in the cryostat at 2 K to stabilize sample and the gate-voltage was ramped up and down several times. AMR(α) measurements were done starting from $V_g = -50$ V to $V_g = +50$ V.

The longitudinal and transversal resistivity were symmetrized and antisymmetrized with respect to magnetic field to obtain $\rho_{xx}(\mu_0 H)$ and $\rho_{xy}(\mu_0 H)$, respectively. $\rho_{\text{AHE}}(\mu_0 H)$ was deduced from $\rho_{xy}(\mu_0 H)$ by subtraction of the linear part, i.e., $\rho_{\text{OHE}}(\mu_0 H)$. Angle-dependent $\rho_{xx}(\alpha)$ was corrected with respect to sample wobbling and offset resistance. All the fitting routines described in the text were carried out with MATLAB and fitting parameters are listed in Tables S1-3 of the Supporting Information S1.

Supporting Information

Supporting Information is available from the Wiley Online Library or from the author.

Acknowledgements

A.K.J. acknowledges financial support from the European Union's Framework Programme for Research and Innovation, Horizon 2020, under the Marie Skłodowska-Curie Grant Agreement No. 847471 (QUSTEC). D.F. thanks S. Rom and T. Saha-Dasgupta from the S. N. Bose National Centre for Basic Sciences (Kolkata, India) for fruitful discussions. The authors are grateful to R. Thelen and the Karlsruhe Nano-Micro Facility (KNMF) for technical support.

Open access funding enabled and organized by Projekt DEAL.

Conflict of Interest

The authors declare no conflict of interest.

Data Availability Statement

The data that support the findings of this study are available from the corresponding author upon reasonable request.

Keywords

anomalous Hall effect, back-gating, iridates, proximity-induced magnetism

Received: August 17, 2023

Published online:

- [1] C. Song, B. Cui, F. Li, X. Zhou, F. Pan, *Prog. Mater. Sci.* **2017**, *87*, 33.
- [2] R. Ramesh, S. Manipatruni, *Proc. Math. Phys. Eng. Sci.* **2021**, *477*, 20200942.
- [3] F. Matsukura, Y. Tokura, H. Ohno, *Nat. Nanotechnol.* **2015**, *10*, 209.
- [4] N. W. Ashcroft, N. D. Mermin, *Solid State Physics*, CBS Publishing Asia LTD, Philadelphia, PA **1976**.
- [5] K. Takiguchi, L. D. Anh, T. Chiba, T. Koyama, D. Chiba, M. Tanaka, *Nat. Phys.* **2019**, *15*, 1134.
- [6] A. J. Grutter, B. J. Kirby, M. T. Gray, C. L. Flint, U. S. Alaun, Y. Suzuki, J. A. Borchers, *Phys. Rev. Lett.* **2015**, *115*, 47601.
- [7] H. Mizuno, K. T. Yamada, D. Kan, T. Moriyama, Y. Shimakawa, T. Ono, *Phys. Rev. B* **2017**, *96*, 214422.
- [8] R. Karplus, J. M. Luttinger, *Phys. Rev.* **1954**, *95*, 1154.
- [9] M. A. Zeb, H. Y. Kee, *Phys. Rev. B* **2012**, *86*, 85149.
- [10] Z. Xiao, Z. Haijun, W. Jing, F. Claudia, Z. Shou-Cheng, *Science* **2012**, *335*, 1464.
- [11] Y. F. Nie, P. D. C. King, C. H. Kim, M. Uchida, H. I. Wei, B. D. Faeth, J. P. Ruf, J. P. C. Ruff, L. Xie, X. Pan, C. J. Fennie, D. G. Schlom, K. M. Shen, *Phys. Rev. Lett.* **2015**, *114*, 16401.
- [12] A. K. Jaiswal, D. Wang, V. Wollersen, R. Schneider, M. Le Tacon, D. Fuchs, *Adv. Mater.* **2022**, *34*, 2109163.
- [13] S. Rom, S. Baidya, S. Bhattacharjee, T. Saha-Dasgupta, *Appl. Phys. Lett.* **2023**, *122*, 021602.
- [14] L. Zhang, Q. Liang, Y. Xiong, B. Zhang, L. Gao, H. Li, Y. B. Chen, J. Zhou, S. T. Zhang, Z. B. Gu, S. Yao, Z. Wang, Y. Lin, Y. F. Chen, *Phys. Rev. B* **2015**, *91*, 35110.
- [15] K. R. Kleindienst, K. Wolff, J. Schubert, R. Schneider, D. Fuchs, *Phys. Rev. B* **2018**, *98*, 115113.
- [16] N. Manca, D. J. Groenendijk, I. Pallecchi, C. Autieri, L. M. K. Tang, F. Telesio, G. Mattoni, A. McCollam, S. Picozzi, A. D. Caviglia, *Phys. Rev. B* **2018**, *97*, 081105(R).
- [17] K. Sen, D. Fuchs, R. Heid, K. Kleindienst, K. Wolff, J. Schmalian, M. L. Tacon, *Nat. Commun.* **2020**, *11*, 4270.
- [18] P. Noël, F. Trier, L. M. Vicente Arche, J. Bréhin, D. C. Vaz, V. Garcia, S. Fusil, A. Barthélémy, L. Vila, M. Bibes, J. P. Attané, *Nature* **2020**, *580*, 483.
- [19] J. Hemberger, P. Lunkenheimer, R. Viana, R. Böhmer, A. Loidl, *Phys. Rev. B* **1995**, *52*, 13159.
- [20] H. Manaka, H. Nozaki, Y. Miura, *J. Phys. Soc. Jpn.* **2017**, *86*, 114702.
- [21] N. Nagaosa, J. Sinova, S. Onoda, A. H. MacDonald, N. P. Ong, *Rev. Mod. Phys.* **2010**, *82*, 1539.
- [22] N. Nagaosa, J. Sinova, S. Onoda, A. H. MacDonald, N. P. Ong, *Rev. Mod. Phys.* **2010**, *82*, 1539.
- [23] D. Feng, G. Jin, *Introduction to Condensed Matter Physics*, World Scientific Publishing Company, Singapore **2005**.
- [24] K. Yosida, *Phys. Rev.* **1957**, *107*, 396.
- [25] R. Karplus, J. M. Luttinger, *Phys. Rev.* **1954**, *95*, 1154.
- [26] L. Berger, *Phys. Rev. B* **1970**, *2*, 4559.
- [27] Y. Ohuchi, J. Matsuno, N. Ogawa, Y. Kozuka, M. Uchida, Y. Tokura, M. Kawasaki, *Nat. Commun.* **2018**, *9*, 213.
- [28] C. Song, B. Cui, F. Li, X. Zhou, F. Pan, *Prog. Mater. Sci.* **2017**, *87*, 33.
- [29] K. Fujiwara, Y. Fukuma, J. Matsuno, H. Idzuchi, Y. Niimi, Y. Otani, H. Takagi, *Nat. Commun.* **2013**, *4*, 2893.
- [30] T. McGuire, R. Potter, *IEEE Trans. Magn.* **1975**, *11*, 1018.

- [31] H. Nakayama, M. Althammer, Y. T. Chen, K. Uchida, Y. Kajiwara, D. Kikuchi, T. Ohtani, S. Geprägs, M. Opel, S. Takahashi, R. Gross, G. E. W. Bauer, S. T. B. Goennenwein, E. Saitoh, *Phys. Rev. Lett.* **2013**, *110*, 206601.
- [32] Z. Lifan, S. Hongkang, L. Kai, L. Zhongzhi, W. Peng, S. Lei, J. Shengwei, X. Hongjun, C. Yanbin, D. Jun, D. Haifeng, X. Ke, X. Jiang, W. Di, *Sci. Adv.* **2022**, *4*, eaa03318.
- [33] S. Bhowal, S. Satpathy, *NPJ Comput. Mater.* **2019**, *5*, 61.
- [34] K. V. Shanavas, S. Satpathy, *Phys. Rev. Lett.* **2014**, *112*, 86802.
- [35] S. E. Barnes, J. Ieda, S. Maekawa, *Sci. Rep.* **2014**, *4*, 4105.
- [36] M. W. Yoo, J. Tornos, A. Sander, L. F. Lin, N. Mohanta, A. Peralta, D. Sanchez-Manzano, F. Gallego, D. Haskel, J. W. Freeland, D. J. Keavney, Y. Choi, J. Strempler, X. Wang, M. Cabero, H. B. Vasili, M. Valvidares, G. Sanchez-Santolino, J. M. Gonzalez-Calbet, A. Rivera, C. Leon, S. Rosenkranz, M. Bibes, A. Barthelemy, A. Anane, E. Dagotto, S. Okamoto, S. G. E. te Velthuis, J. Santamaria, J. E. Villegas, *Nat. Commun.* **2021**, *12*, 3283.
- [37] R. Winkler, *Spin-Orbit Effects in Two-Dimensional Electron and Hole Systems*, Springer, New York **2003**.
- [38] F. Gallego, J. Tornos, J. I. Beltran, A. Peralta, J. Garcia-Barriocanal, G. Yu, C. Rojas, C. Munuera, M. Cabero, D. Sanchez-Manzano, F. Cuellar, G. Sanchez-Santolino, Z. Sefrioui, A. Rivera-Calzada, F. J. Mompean, M. Garcia-Hernandez, C. Leon, M. del Carmen Muñoz, J. Santamaria, *Commun. Mater.* **2023**, *4*, 36.
- [39] D. Xiao, M. C. Chang, Q. Niu, *Rev. Mod. Phys.* **2010**, *82*, 1959.
- [40] Q. Lu, P. Li, Z. Guo, G. Dong, B. Peng, X. Zha, T. Min, Z. Zhou, M. Liu, *Nat. Commun.* **2022**, *13*, 1650.
- [41] Z. Fang, N. Nagaosa, K. S. Takahashi, A. Asamitsu, R. Mathieu, T. Ogasawara, H. Yamada, M. Kawasaki, Y. Tokura, K. Terakura, *Science* **2003**, *302*, 92.
- [42] T. Nan, T. J. Anderson, J. Gibbons, K. Hwang, N. Campbell, H. Zhou, Y. Q. Dong, G. Y. Kim, D. F. Shao, T. R. Paudel, N. Reynolds, X. J. Wang, N. X. Sun, E. Y. Tsybal, S. Y. Choi, M. S. Rzechowski, K. Y. Baek, D. C. Ralph, C. B. Eom, *Proc. Natl. Acad. Sci. USA* **2019**, *116*, 16186.
- [43] A. S. Patri, K. Hwang, H. W. Lee, Y. B. Kim, *Sci. Rep.* **2018**, *8*, 8052.
- [44] H. Weng, R. Yu, X. Hu, X. Dai, Z. Fang, *Adv. Phys.* **2015**, *64*, 227.
- [45] R. Nishino, T. C. Fujita, M. Kawasaki, *APL Mater.* **2022**, *10*, 081104.
- [46] J. Zhao, B. Jiang, J. Yang, L. Wang, H. Shi, G. Tian, Z. Li, E. Liu, X. Wu, *Phys. Rev. B* **2023**, *107*, L060408.
- [47] A. K. Jaiswal, R. Schneider, R. Singh, D. Fuchs, *Appl. Phys. Lett.* **2019**, *115*, 031904.